Cement and Concrete Research 152 (2022) 106683

Contents lists available at ScienceDirect

Cement and Concrete Research

journal homepage: www.elsevier.com/locate/cemconres

Phase evolution, micromechanical properties, and morphology of calcium (alumino)silicate hydrates C-(A-)S-H under carbonation

Rotana Hay [a], Jiaqi Li [b], Kemal Celik [a,*]

[a] Division of Engineering, New York University Abu Dhabi, Abu Dhabi, P.O. Box 129188, United Arab Emirates
[b] Department of Civil and Environmental Engineering, University of California at Berkeley, 94720 Berkeley, United States

ARTICLE INFO

Keywords:
Nanoindentation
CO_2 uptake
Cement
Green concrete
C-(A-)S-H

ABSTRACT

The study explored the chemical, micromechanical, and morphological evolution of the principal binding phases of Portland cement under carbonation. Accelerated carbonation under 20% CO_2 at 80% relative humidity was applied on C-(A-)S-H powders until equilibrium. The crystallinity of C-(A-)S-H disappeared due to decalcification and subsequent formation of highly polymerized silica gels. A high carbonation content (33.4–35.2%) was achieved. $CaCO_3$ polymorphs dominated by aragonite and vaterite were observed as the main carbonation products. A significant reduction in the indentation elastic modulus was revealed in compacts produced with carbonated powders. In contrast, compacts followed by carbonation attained an improved micromechanical property, attributed to a reinforcing action of integral $CaCO_3$ nanocrystallites and pore-filling effects. The carbonated C-(A-)S-H powders achieved an overall lower pore volume and exhibited a more fibrous morphology characterized by thin foils of silica gels bound with $CaCO_3$ crystals to form agglomerates.

1. Introduction

Carbonation is inevitable for all Portland cement (PC)-based concrete structures exposed to the natural environment. The mechanism involves the diffusion of CO_2 into the concrete pores, its dissolution in the pore solution to form HCO_3^- and CO_3^{2-}, dissolution of $Ca(OH)_2$ and anhydrous phases as the pH reduces, decalcification of calcium silicate hydrate (C-S-H), and formation of carbonates and secondary products [1,2]. Calcium carbonate ($CaCO_3$) polymorphs in the form of calcite, aragonite, and vaterite were observed in carbonated concrete matrices along with C-S-H of reduced Ca/Si ratios and silica gels as the by-products [3–5]. The carbonation rate is controlled by the diffusivity, which in turn is governed by the porosity and exposure condition [2]. While the binder content and type, water-to-binder ratio, and early-age curing influence the pore system, CO_2 concentration, relative humidity (RH), and surface finishes such as tiles also affect the CO_2 diffusivity and ultimately the carbonation rate [2,6,7]. The RH level within the pores also influences the carbonation of the matrix constituents with preferential carbonation of C_3S and C_2S at a low RH, and of $Ca(OH)_2$ at a high RH (95%) [8].

Carbonation induces physicochemical and mechanical changes to the concrete. The total porosity of PC-based pastes was found to be reduced [9], attributable to the 11.2% higher molar volume of $CaCO_3$ in comparison to that of $Ca(OH)_2$ [10,11]. Despite this fact, a redistribution of pore size was also observed [12]. Capillary porosity in size range of 2–7 nm increased in a well-carbonated mortar [13], possibly due to the decalcification and dissolution of the cement phases [10]. Carbonation was also found to cause irreversible shrinkage in concrete [14], attributed to the dissolution of $Ca(OH)_2$ crystals under pressure [15]. Other researchers also contributed the shrinkage phenomenon to the structural change and decomposition of C-S-H [16]. As a result of the porosity reduction, carbonation markedly increased the compressive and tensile strengths of PC-based mortars [1]. Despite exhibiting a more brittle failure, carbonated concrete exhibited a higher strength and modulus of elasticity with increasing cement content [17]. Conversely, carbonation induces adverse effects on concrete durability. CO_2 neutralizes the pore solution, reduces the pH, and subsequently depassivates the embedded rebar to initiate active corrosion [18]. Measurements on carbonation depths, corrosion potentials, and gravimetric mass losses revealed that corrosion started when the carbonation depth reached 80% of the concrete cover [19,20]. Once initiated, the corrosion activity increases in carbonated concrete and is controlled mainly by the remaining unneutralized region, which is defined as the concrete cover less the carbonation front [21,22].

* Corresponding author.
E-mail address: kemal.celik@nyu.edu (K. Celik).

https://doi.org/10.1016/j.cemconres.2021.106683
Received 14 June 2021; Received in revised form 17 October 2021; Accepted 29 November 2021
Available online 15 December 2021

Fundamental to the carbonation process in concrete is the physical and chemical alteration of the principal binding phase of PC, namely calcium (alumino)silicate hydrates or C-(A-)S-H. It was found that the carbonation of C-S-H in liquid formed calcite and silica gels, and the mechanism involved the decomposition of C-S-H to calcite and Ca-bearing silica gels (of low Ca/Si ratios), which further transformed into calcite and pure silica gels [23]. Similarly, in hydrated cement pastes, C-S-H under carbonation is decomposed to calcium carbonate ($CaCO_3$) and silica gels [24]. $CaCO_3$ polymorphs (aragonite, vaterite, and calcite) were found as dense masses intermixed with the gel fibrils and around the partially carbonated $Ca(OH)_2$ [1,25]. In the early stage of carbonation, C-S-H with reduced Ca/Si was formed, and carbonation progressively occurred on the outer product and outer regions of inner product C-S-H [25,26]. C-S-H of low Ca/Si ratios and the incorporation of magnesium, which induced cross-linking, was found to be more resistant to carbonation [27]. The carbonation of C-S-H and $Ca(OH)_2$ occurred simultaneously but at a slower rate for the residual $Ca(OH)_2$ [28] as the underlying crystal became less accessible [29]. At a high carbonation degree (>25%), shrinkage of tobermorite [30,31], a structural analogy of C-(A-)S-H, was observed due to the dissolution of calcium from the interlayer and the double-chain silicate structures [32]. C-S-H in cement pastes also experiences carbonation shrinkage due to its structural change to sheet-like morphologies at Ca/Si of 1.2 and its subsequent decomposition to form silica gels [16].

Due to the phase assemblage of hydration products in clinker-based matrices, carbonation kinetics of C-(A-)S-H is a complex phenomenon. Exposure to CO_2 at an early stage of hydration induced carbonation of Ca^{2+} leached from calcium silicates [33] with the prevalent formation of amorphous $CaCO_3$ [34]. As the hydration progresses, the CO_2 diffusion control imparted by the dense paste matrix and further matrix densification by $CaCO_3$ will impede carbonation and decalcification of C-(A-)S-H, and not all the decalcified Ca could be transformed into carbonates due to its containment in the residue and reaction products [35]. The incorporation of 20% fly ash formed C-(S-)A-H of low Ca/Si ratios and led to the preferential formation of calcite in comparison to vaterite in pastes produced with unblended or slag-blended cement [36,37]. Contradictory to a previous report [14], volume increase from the transformation of $Ca(OH)_2$ to $CaCO_3$ formation was found to dominate the possible shrinkage induced by decalcination of C-(A-)S-H, leading to expansion in both PC and fly ash-blended binder matrices [38]. The volume expansion and intermingling of $CaCO_3$ with the hydration products densified and stiffened the matrix, resulting in an improved composite performance [37,39,40]. Environmental factors such as CO_2 concentration and relative humidity (RH) were shown to greatly influence the carbonation rate [41,42]. However, under 3–20% CO_2, 20 ± 2 °C, and 74 ± 2% RH, the distribution of the three $CaCO_3$ polymorphs was noted to be dependent on the degree and duration of carbonation, irrespective of the CO_2 concentration [41]. Also, the formation of metastable vaterite and aragonite, instead of calcite, was promoted at 3% CO_2 in the carbonation of portlandite and ettringite, while vaterite was the dominant carbonation product from C-(A-)S-H [43].

The prevalence of concrete incorporated with traditional supplementary cementitious materials (SCMs), including fly ash, slag, and natural pozzolans [44–46], and the emergence of promising alternative binders such as limestone calcined clay (LC^3) [47–51] raise the criticality of carbonation. The resulting lower clinker content and the associated pozzolanic reactions in these composites reduce the content of the available $Ca(OH)_2$, leading to their vulnerability to carbonation. A high replacement level of fly ash in excess of 30% was found to cause more aggressive carbonation in concrete [2,52]. Despite a reduction in the total porosity, large pore sizes > 30 nm were observed to increase more significantly in carbonated pastes produced with slag and fly ash [12]. Composites produced with high-volume SCMs contain less Ca $(OH)_2$, thus resulting in coarsening of the matrix pore structure under carbonation [10]. Gas permeability was increased in carbonated concrete produced with high volume fly ash [53]. Despite experiencing a deeper carbonation depth [54–56], concrete produced with fly ash or slag generally was shown to exhibit a strength enhancement upon carbonation [57–59].

The decalcination of C-(A-)S-H would be expected to reduce the mechanical property in composites produced with slag and fly ash due to their reduced $Ca(OH)_2$ content, less $CaCO_3$ formation, and reduced matrix densification. However, as discussed above, despite their coarser pore size redistribution, these composites generally exhibit an improved mechanical performance. As C-(A-)S-H is their main hydration product, it is hypothesized that this phenomenon could potentially be explained by its fundamental change and the interaction of the carbonation products. Thus, this study aims to answer the question by unraveling the characteristics of C-(A-)S-H under carbonation and its linkage to the bulk properties of concrete. The evolution of the chemical, micromechanical, and morphological properties of C-(A-)S-H at carbonation equilibrium was monitored. The incorporation of aluminum into the C-(A-)S-H binding phase and its effects on carbonation were also investigated. A series of testing programs was performed. Thermal gravimetric analysis (TGA), X-ray diffraction (XRD), and Raman spectroscopy were conducted to comprehend the chemical evolution of both the uncarbonated and carbonated C-(A-)S-H samples and their CO_2 absorption capacities. Nanoindentation on compacts was used to characterize their micromechanical properties. Meanwhile, nitrogen (N_2) gas adsorption and electron microscopy were used to investigate the physical and morphological change of the samples, respectively. The outcome of the study contributes to a more in-depth understanding of concrete aging under carbonation.

2. Experimental section

2.1. Materials

C-(A-)S-H samples were synthesized under a N_2-filled glovebox by mixing SiO_2 (Aerosil 200), CaO, and/or $CaO{\cdot}Al_2O_3$ powders at stoichiometric values with a bulk Ca/(Al + Si) molar ratio fixed to 1 and bulk Al/(Al + Si) molar ratios set at 0 and 0.1. The samples were annotated as A0 or C-S-H and A1 or C-A-S-H, respectively. In neat Portland cement pastes, C-(A-)S-H is a non-nonstoichiometric compound with Ca/Si varying between 1.2 and 2.3 [60,61]. A lower Ca/(Al + Si) adopted in this study is applicable to pastes incorporated with supplementary cementitious materials (SCMs) such as slag and fly ash which lead to a reduction in Ca/(Al + Si) and incorporation of Al into the C(A-)S-H products [62–64]. Alkali-activated slag and Ca-rich aluminosilicates were also found to contain low Ca/(Al + Si) ratios (0.8–1.5) [1,65–67]. As part of the synthesis procedure, the water content was fixed at 45 times, and the mixtures were cured at 80 °C for three months to achieve a quick equilibrium [68]. The solid C-(A-)S-H precipitates were extracted with 0.45 μm nylon filters in N_2-filled desiccators and conditioned with NaOH pellets for 14 days. The samples were subsequently freeze-dried and sealed to prevent carbonation. Energy-dispersive X-ray spectroscopy (EDS) analyses of pressed pellets confirmed that the C-(A-)S-H precipitates followed the stoichiometry of the input reactants.

2.2. Sample conditioning and compact preparation

Conditioning was applied on the C-(A-)S-H samples until a weight equilibrium under three regimes: (i) room temperature (22–24 °C) at 11% RH achieved by saturated lithium chloride solution [1,69,70] (A0, A1), (ii) room temperature (22–24 °C) at 75% RH as controlled by saturated sodium chloride solution (for C-S-H only, A0*), and (iii) carbonation under 20% CO_2, 30 °C at 80% RH concentration until equilibrium as indicated by a weight stability (A0-C, A1-C). The 11% RH was adopted to achieve a monolayer of water on the C-(A-)S-H surface to aid compaction [69] without capillary condensation [71]. Taylor [1] recommended using this level of RH to determine chemically bound water in C-S-H gels, and the condition has been adopted by other

researchers to investigate the micromechanical properties of C-(A-)S-H granules [69,70,72]. Meanwhile, the 75% RH was to simulate the typical moisture condition of concrete [73]. Also, the level was similar to the RH adopted in the carbonation condition so as to isolate the influence of the moisture content in C-(A-)S-H on its micromechanical properties. For the carbonation regime, the high CO_2 concentration was to accelerate the carbonation of C-(A-)S-H, thus mimicking a long-term operational condition or exposure to concentrated CO_2 such as the condition under flue gas. This is in line with other studies where the CO_2 concentration, temperature, and RH in the vicinity of the values adopted in this study were implemented to accelerate the carbonation of cementitious materials [37,74–77]. The materials in a granular form were first exposed to the carbonation regime to achieve complete carbonation and to enable an investigation into the intrinsic characteristics of C-(A-)S-H. In preparation for nanoindentation, the conditioned or carbonated powders were pressed to a maximum pressure of 95 MPa into compacts. The pressure level produced compacts that yielded modulus distributions corresponding to various phases of the input synthetic calcium silicate hydrates [70]. A higher pressure level (>200 MPa) may induce preferred orientation which increases the indentation modulus [78]. More information on the sample preparation and parameters affecting the micromechanical properties of compacted C-(A-)S-H could be found in our previous work [79]. Yet, in concrete, the carbonation of C-(A-)S-H occurs as part of the matrix. Thus, to elucidate the influence of matrix confinement on the micromechanical properties of C-(A-)S-H under carbonation, the compacted A0* was subsequently carbonated under 20% CO_2, 30 °C at 80% RH for 6 months (longer than required for equilibrium) before nanoindentation, and the sample was annotated as A0*-P-C. Table 1 summarizes all the samples used in the current study.

2.3. Phase identification

Both the C-(A-)S-H powder samples and carbonated compact (A0*-P-C) were used for thermo-gravimetry/differential thermal analysis with SQ600 TG/DTA series with temperature regulated from 30 to 1000 °C at a constant ramping rate of 10 °C/min under a N_2 gas flow of 100 ml/min. The samples were also subjected to XRD with PANalytical Empyrean of a Cu Kα radiation source. The data acquisition was performed under 40 mA and 40 kV with 2θ ranged from 3–70° at a step of 0.013° and an acquisition time of 350 s. Raman spectra for the compact samples were acquired using a confocal Raman microscope (alpha300 RA from WITec GmbH, Ulm, Germany). A laser source with a wavelength of 488 nm was adopted, and the detector was set at 1800 lines/mm for high resolution scanning between 100 cm^{-1} and 1200 cm^{-1}. A silicon wafer with an emission band at 520 cm^{-1} was used for signal calibration.

2.4. Micromechanical properties

Grid indentation was performed with a Keysight G-200 nanoindenter on the C-(A-)S-H compacts mounted on aluminum platforms using a thermoplastic adhesive. The diamond Berkovich tip was chosen, and the hardness and modulus properties of the material were measured at a target indentation depth [80,81], which was chosen to be 350 nm to achieve an optimum interaction volume larger than the nanogranular globules [82]. The corresponding peak load was held for 10 s to mitigate creep and thermal drift effects, and the elastic modulus value was estimated from the respective unloading curve. A total of 72 points were implemented on each sample. More information on the operational parameters and formulae to derive the modulus could be found in [79].

Table 1
Sample annotations and corresponding materials, conditioning and compaction requirements.

Annotation	Material	Conditioning/carbonation	Compaction
A0	C-S-H	11% RH	After conditioning
A1	C-A-S-H (Al/(Al + Si) = 0.1)	11% RH	After conditioning
A0*	C-S-H	75% RH	After conditioning
A0-C	C-S-H	20% CO_2, 30 °C at 80% RH	After carbonation
A1-C	C-A-S-H (Al/(Al + Si) = 0.1)	20% CO_2, 30 °C at 80% RH	After carbonation
A0*-P-C	C-S-H	75% RH followed by compaction and 20% CO_2, 30 °C at 80% RH	Before carbonation

2.5. Nitrogen gas adsorption

A surface analyzer (3Flex by Micromeritics, USA) was used to determine the nitrogen (N_2) gas adsorption characteristics of A0, A1, A0-C, and A1-C before compaction and ground A0*-P-C. The specific surface area (SSA) of hydrated cement pastes was shown to depend on the conditioning or degassing method [83–85], relative humidity [86], matrix inclusions [87,88], and the presence or absence of narrow ink-bottle pores in the tested materials [89]. In this study, all the C-(A-)S-H samples were degassed under a pressure of 0.1 mmHg at 150 °C for 10 h to remove the surface moisture [70] before the N_2 adsorption-desorption measurements. The procedure created the same initial condition for all the samples, thus allowing for a comparative analysis between them. The adsorption and desorption responses were obtained by varying the chamber pressure between 1.3×10^{-9} and 1 with respect to the saturation pressure of N_2 (P_o) at −196 °C, the liquid temperature of N_2. The response curves were used to derive the cumulative pore volume and specific surface area (SSA).

2.6. Morphologies with scanning electron microscopy (SEM) and transmission electron microscopy (TEM)

The morphologies of selected samples were characterized with both SEM and TEM. SEM was performed under the backscattered electron mode with Quanta FEG 450 set at 5–10 kV and 3 nA. For TEM analyses, the samples were ground and suspended in ethanol with ultrasonication. A solution of approximately 0.5 μl was deposited on a Holey carbon film on 400 mesh copper grids which were subsequently dried under vacuum for at least 12 h before TEM to improve sample stability and limit sample damage due to electron beam-hydrocarbon interaction. Bright-field images and selected area diffractions (SAD) were obtained under 200 kV accelerating voltage.

3. Results

3.1. Phase characteristics

Fig. 1 provides the relative sample weight and differential weight loss data of all the samples under TGA. In Fig. 1 (a), endothermic peaks between 80 and 145 °C were observed in both A0 and A1 and corresponded to dehydration of the adsorbed water from the interlayer or structure of the C-(A-)S-H samples [68,90]. Broad peaks at around 450 °C occurred in A0 and A1 and were attributed to the thermal decomposition of the synthetic C-(A-)S-H [68]. The peak could not be assigned to $Ca(OH)_2$ considering its broad nature and absence of $Ca(OH)_2$ peaks in the XRD spectra (to be shown below). A weak peak in the vicinity of 810 °C could be attributed to the transformation of C-(A-)S-H to wollastonite ($CaSiO_3$) [91]. Compared to A0, there was no marked difference in the decomposition characteristics of A1 except for peak broadening for dehydration at 165 °C and C-S-H decomposition peak at 450 °C, which indicated an enhanced order of A1. A0* was noted to exhibit an early dehydration peak at approximately 50 °C, attributed to: (i) drying of condensed water (induced by conditioning at a higher RH of 75%) from gel nanopores between C-(A-)S-H globules [92–94], and (ii) dehydration of moisture from partial carbonation and decalcification of

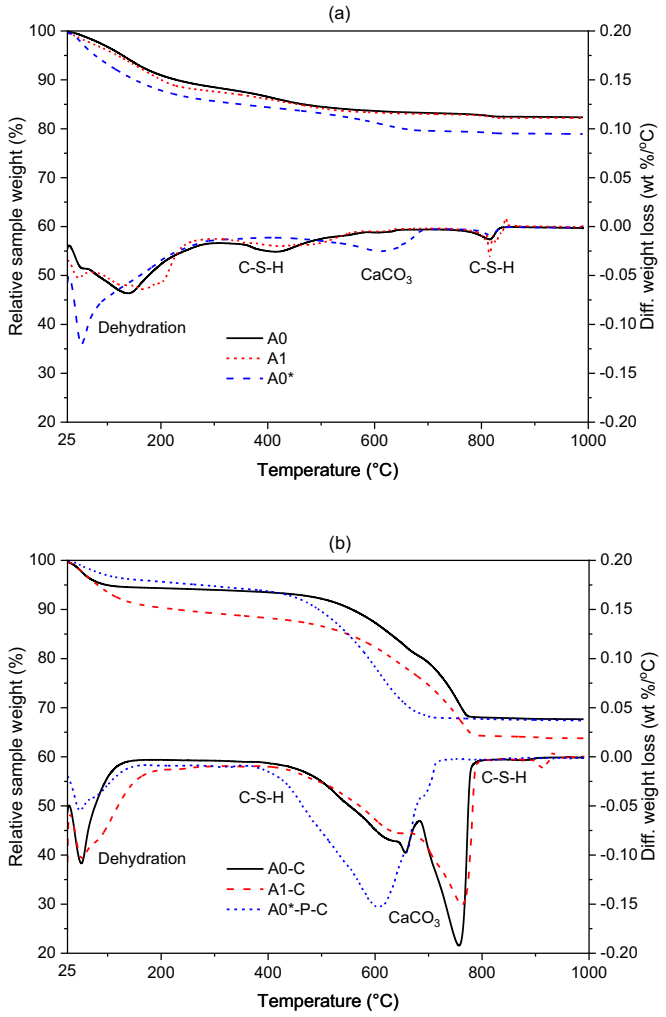

Fig. 1. TGA results for C-S-H (A0) and C-A-S-H (A1) under: (a) 11% and 75% RH, and (b) 20% CO_2 at 80% RH (annotated by C) (Data for A0, A0* and A1 were published in a previous work [79] and reproduced here for easy reference.)

C-(A-)S-H [95], which formed calcium carbonate, amorphous silica gel, and water [29]. The presence of an endothermic peak at 625 °C, which is assigned to $CaCO_3$ [96], confirmed the partial carbonation of A0*.

Carbonation led to more intense dehydration peaks within a smaller temperature range (~50 °C) in A0-C, A1-C, and A0*-P-C, attributable to the decalcification of C-(A-)S-H and the associated formation of calcium carbonate, amorphous silica gels, and water. This physical water was found to be retained during carbonation at the ambient temperature [29] and was postulated to be released upon heating. Complete carbonation of C-(A-)S-H and its phase transformation were noted through the disappearance of the broad peaks in the vicinity of 450 °C and 810 °C in all the samples. The formation of metastable $CaCO_3$ polymorphs (vaterite, aragonite, and amorphous $CaCO_3$) could be identified with their early decomposition starting from 400 °C as compared to the 600–800 °C range for the decomposition of calcite [96,97], consistent with findings by other researchers [27,29]. Interestingly, A0*-P-C exhibited an even earlier onset of the endothermic peak assigned to $CaCO_3$. The high RH in both the conditioning and carbonation regimes for A0*-P-C was postulated to form more vaterite, which exhibits a poor phase stability by both decomposition and transformation to calcite at around 400 °C [98,99]. The tangential method was used between 400 and 800 °C to yield a CO_2 content of 35.2% for A0-C, 33.4% for A1-C, and 34.4% for A0*-P-C with respect to sample weight at 1000 °C. Thus, despite the cross-linking with the incorporation of Al in C-A-S-H [68], the three samples exhibited no noticeable difference in their susceptibility to carbonation and CO_2 sequestration content. All the aluminum sites were found to deteriorate under carbonation and integrate as tetrahedral $Al(–OSi)_4$ units in the amorphous silica [95].

The normalized XRD results (Fig. 2) show that the longer-range order of C-A-S-H (A1) with Al incorporation was observed with an increase in the sharpness and number of the diffraction peaks in comparison to A0, consistent with findings in [68,100]. The 2θ angles of the basal peaks in A1 were generally higher in comparison to that of C-S-H (A0). This indicated its reduced interlayer spacing, attributable to an improved cross-linking in C-A-S-H with Al incorporation [68,101]. Enhanced peak intensity and sharpness in A0* were noted and indicated its higher-order due to saturation of the interlayer with water at high RH conditioning [93,102]. Based on small-angle neutron scattering, a well-defined peak was also observed for C-S-H with a higher water content [103]. $Ca(OH)_2$ was not observed in both A0 and A1, signifying the phase purity of the two samples. Consistent with the TGA results, peaks corresponding to vaterite and aragonite were also observed in A0* due to their partial carbonation. Carbonation caused a significant modification of the crystal structure in A0-C, A1-C, and A0*-P-C. The peaks assigned to C-(A-)S-H disappeared due to their decalcification under carbonation, whereby the calcium from the interlayer and defect sites was removed and reacted with dissolved CO_2 (HCO_3^- and CO_3^{2-}) to form polymorphs of $CaCO_3$, including calcite, vaterite, and aragonite [95,104]. The XRD spectrum results confirmed the presence of $CaCO_3$ polymorphs and calcite, with aragonite being the most dominant carbonation phase in A0-C and A1-C. Although the carbonation phases were found to be dependent on the carbonation duration, Ca/Si ratios, and pH, a preferential formation of aragonite was also observed in aged C-S-H samples in previous studies [105,106]. In this study, it is also noted that the initial RH of the samples also influenced the carbonate pathway, with a higher RH leading to more formation of vaterite, as reflected by its more prominent peaks in A0*-P-C. Also, the decalcification causes a negative charge imbalance in the C-(A-)S-H structure, which induces the formation of Si-O for charge equilibrium [16]. The Si-O groups subsequently condensated to form Si-O-Si. A broad peak in the vicinity of 21° 2θ (highlighted by a dashed box) assigned to the amorphous silica gels was observed in the carbonated samples due to the polymerization and the resulting formation of the amorphous silica phases. The peak broadening was less apparent in A1-C in comparison to A0-C and A0*-P-C, possibly due to enhanced polymerization with the incorporation of tetrahedral $Al(-OSi)_4$ units in the silica chains in A1-C [95].

All bands below 400 cm^{-1} of the normalized Raman spectrum results shown in Fig. 3 were ascribed to Ca-O vibrations [107], with a broad peak in the region of 305.4 cm^{-1} assigned to the Ca-O polyhedral lattice vibration [108]. A band at 356 cm^{-1} corresponding to Ca-O vibration in $Ca(OH)_2$ [109] was not evident in the samples, thus confirming that $Ca(OH)_2$ was not formed in both the C-(A-)S-H samples. The peak at 444.1 cm^{-1} was due to the vibration of non-bridging oxygen atoms of SiO_4 [110]. The peak at 600–700 cm^{-1} was due to the bending vibration of the Si-O-Si in the C-(A-)S-H, while the peak in the vicinity of 1000 cm^{-1} was assigned to Si-O stretching in Si-tetrahedra of Q^2 sites [107,111]. The enhanced cross-linking with the incorporation of Al was reflected by a weak shoulder at 1040 cm^{-1} corresponding to Si-O vibration at Q^3 sites [110]. The prolonged carbonation regime led to the decomposition of the C-(A-)S-H and the disappearance of peaks corresponding to vibration and stretching of Si-O bonds. The reduction in the relative peak intensity at 600–700 cm^{-1} and 1040 cm^{-1} in A0* confirmed its partial carbonation. The absence of Q^2 in A0-C, A1-C, and A0*-P-C suggests an increase in the silica polymerization degree due to carbonation. The C-O spectrum with a peak at 1082.8 cm^{-1} [107,110] was evident in all the samples due to their partial or full carbonation with the associated formation of $CaCO_3$ polymorphs. The peak intensity in the vicinity 1082.8 cm^{-1} became more prominent in A0-C, A1-C, and A0*-P-C

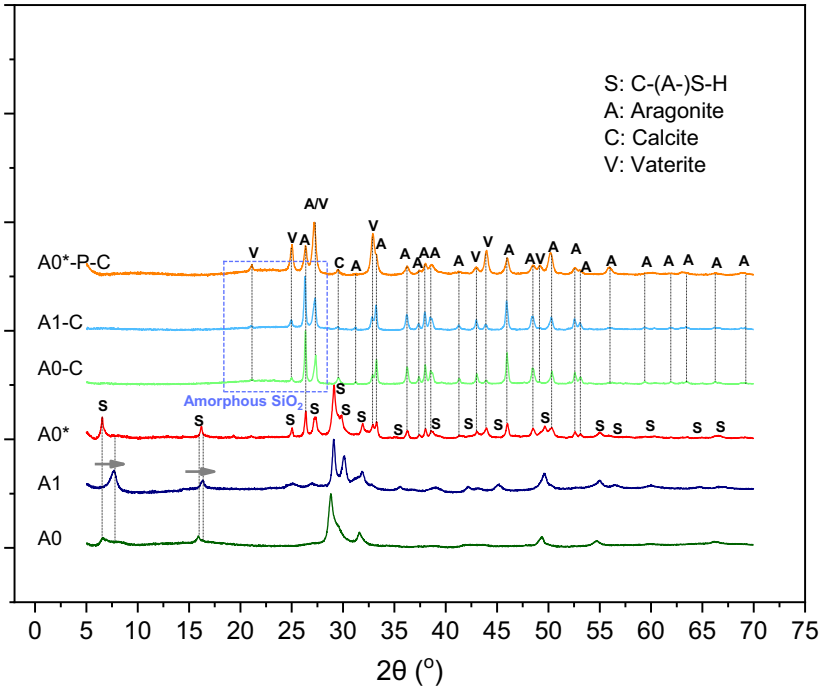

Fig. 2. XRD results for C-S-H (A0) and C-A-S-H (A1) under (i) 11% RH and (ii) 20% CO_2 at 80% RH (annotated by C).

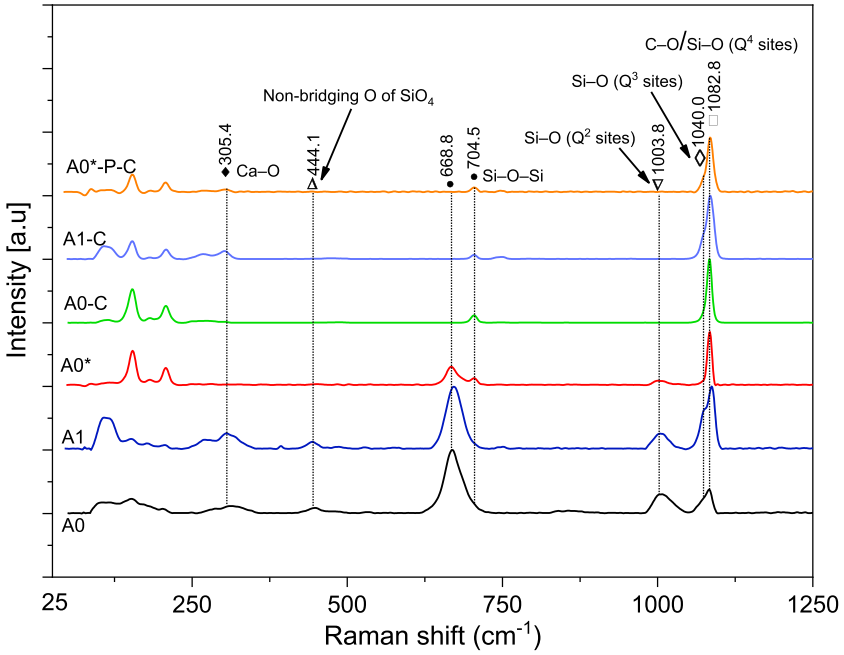

Fig. 3. Normalized Raman spectrum data for C-S-H (A0) and C-A-S-H (A1) under (i) 11% RH and (ii) 20% CO_2 at 80% RH (annotated by C)

relative to the intensities of other peaks, attributed to the increase in their carbonation levels. The shoulder at 1040 cm^{-1} was retained in the A1-C sample, attributable Al incorporation to form tetrahedral $Al(-OSi)_4$ in the amorphous silica [95]. The Q^4 deformation modes of silicate tetrahedron in the range of 1000–1200 cm^{-1} [112] could have overlapped with the signal of C-O, leading to a high relative intensity of the peak in the region.

3.2. Micromechanical properties with nanoindentation

The elastic modulus data presented in relative frequency plots for both the A0 and A1 samples (Fig. 4) revealed that the indentation modulus exhibited a single modal distribution, indicating a homogenous distribution of phases within the matrices. The slight skewness and the data spread were attributed to the presence of porosity. Under 11% RH, A1 achieved an average elastic modulus value of 6.5 GPa or 14% higher than the level in A0. The superior micromechanical property in A1 or C-A-S-H was due to: (i) improved cross-linking with the incorporation of

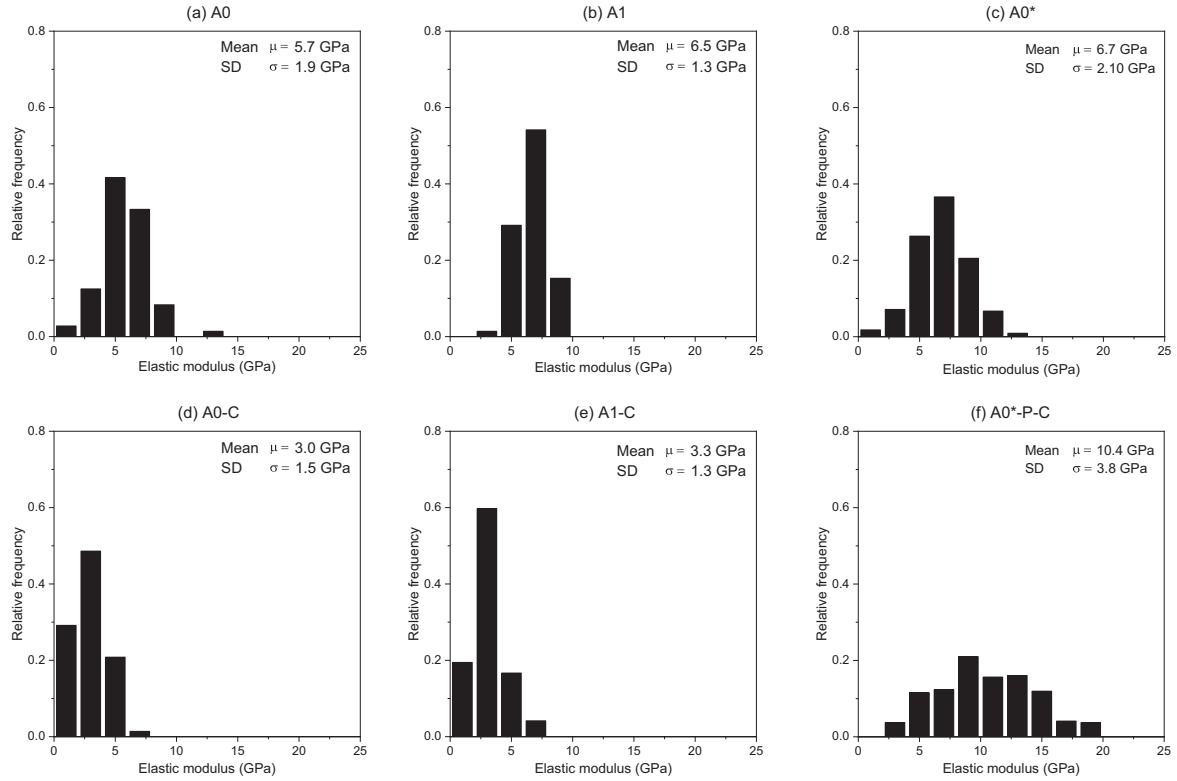

Fig. 4. Nanoindentation data for: (a) C-S-H, (b) C-A-S-H under 11% RH at 22–24 °C (A0 and A1, respectively), (c) C-S-H under 75% RH at 22–24 °C (A0*), (d) C-S-H, (e) C-A-S-H, and (f) compacted A0* under 20% CO_2 at 80% RH and 30 °C (A0-C, A1-C, and A0*-P-C, respectively) (Data for A0 and A1 were published in a previous work [79] and reproduced here for easy reference.)

Al, thus leading to improved resistance to compression of the nanocrystalline C-(A-)S-H [101], and (ii) better compactibility of the C-A-S-H platelets to result in enhanced matrix densification [79]. The improved consolidation and reduction in the porosity could also explain the lower standard deviation observed in A1. C-S-H conditioned at 75% RH (A0*) achieved an average elastic modulus of 6.9 GPa or 21.0% higher than the level of A0, attributable to improved consolidation of C-S-H grains at the higher RH [79], and the saturation of the fractal structure with the associated increase in the capillary stresses and resistance to deformation [102]. With the target penetration depth of 350 nm, the interaction volume was estimated to have a linear length of 1400 nm based on a relationship proposed in [113,114]. The value is larger than the gel and capillary pores, which are in the range of 1–100 nm [93,94]. Thus, the shown elastic modulus values represented an aggregate effect of all the pore systems and are naturally lower than the intrinsic elastic modulus data obtained from high-pressure XRD and atomic force microscopy [79,101,115–118].

Carbonation of the C-(A-)-S-H powders and subsequent compaction for indentation led to a significant reduction in the micromechanical property of the compacts. A0-C and A1-C exhibited an average modulus of 3.0 and 3.3 GPa, respectively. These values corresponded to a reduction of 47% and 62% from those of the uncarbonated samples. The reduction could be mainly ascribed to the formation of silica gels with a lower elastic modulus compared to that of the original C-(A-)S-H and the resulting low binding property of the carbonated powder. In contrast, the carbonated compact of C-S-H (A0*-P-C) attained a 50.7% enhancement to its elastic modulus from 6.7 GPa to 10.4 GPa. Although the frequency plot for A1 compacted and carbonated is not given (i.e., A1*-P-C), its average elastic modulus increased to 10.1 GPa upon carbonation as compared to 7.9 GPa for C-A-S-H conditioned at 75% RH without carbonation [79]. Fig. 5 provides a summary of the indentation elastic modulus and standard deviation values of the C-(A-)S-H samples with the different conditioning regimes. As the RH regime of A0* and

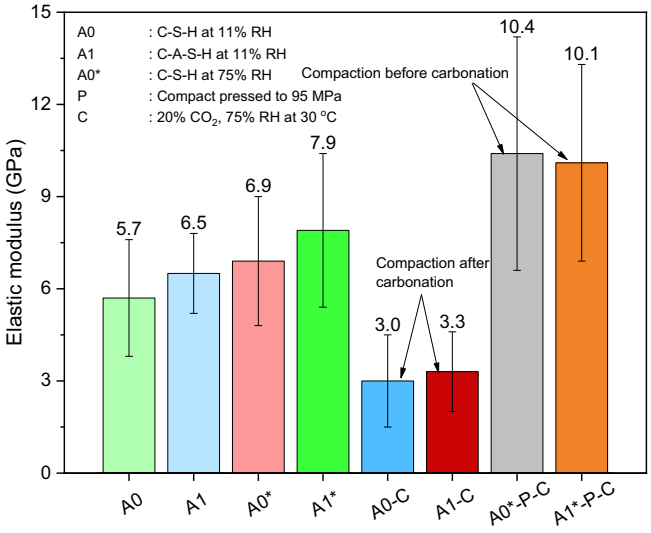

Fig. 5. Summary of the indentation elastic modulus and standard deviation values of C-(A-)S-H samples with different conditioning regimes

A0*-P-C was maintained in the range of 75–80%, the micromechanical property enhancement was attributed to other factors rather than an increase in the moisture content in C-(A-)S-H: (i) the formation of $CaCO_3$ polymorphs through CO_2 uptake and the associated pore filling, and (ii) the higher elastic modulus of $CaCO_3$ (in the range of 79.3–91.7 GPa) [119,120]. Carbonated cement pastes were found to consistently exhibit a higher elastic modulus and hardness after carbonation [40,121]. The lower modulus values for the C-(A-)S-H samples carbonated before compaction in comparison to those carbonated after compaction implies

that the intrinsic mechanical properties of C-(A-)S-H (i.e., without $CaCO_3$ polymorphs and their pore filling effects) were reduced due to decalcification and the associated density reduction. It follows that analogous to the carbonated compact, a carbonated concrete matrix would also experience an improvement to the mechanical properties under carbonation. The single modal distribution of the frequency plots also indicates that the $CaCO_3$ polymorphs were of nano to micro sizes and evenly distributed within the C-(A-)S-H globules, thus preventing a peak separation of the reaction products. Excluding the contribution of $CaCO_3$ to the mechanical properties, the true micromechanical properties of silica gels are expected to be even lower than the presented mean values.

3.3. Morphologies

The C-(A-)S-H samples were mainly characterized by fibrillar or foil-like agglomeration without a clear crystal structure (Fig. 6), similar to what was observed by other researchers [100,122–124]. Large micron-size needle-like structures were also noted in the C-S-H sample, possibly due to the agglomeration and folding of the fractal foils [125]. There was no apparent change in the morphology of A0*, which was conditioned under 75% RH. Interestingly, the C-A-S-H sample was dominated by more dispersed globules of smaller sizes. The incorporation of Al at 80 °C was shown to enhance the cross-linking and polymerization of C-A-S-H [68]. Thus, the smaller agglomeration of A1 globules could be attributed to the presence of Al in the aqueous environment affecting nucleation and charge balancing in the precipitates. Although more investigation is warranted, such balancing was postulated to reduce electrostatic force at the cross-linking sites and chain ends, resulting in less interaction with the neighboring sheets and smaller globule sizes.

Fig. 7 reveals that carbonation led to a more fibrillar morphology of both A0-C and A1-C. The decalcification from the interlayer and the defect sites induced the polymerization of silica gels of lower stiffness and resulted in a feather-like foil. The matrices of the carbonated samples were interspersed with small-size carbonation products of rod-like aragonite [126] and spherulite-like vaterite of submicron sizes [127], consistent with the XRD results. EDX spot analyses (inset) confirmed that incorporation of C, with varying contents of Ca, Si, and/or Al depending on the spot location (within $CaCO_3$ or polymerized silica). In addition, the $CaCO_3$ crystals were observed to form dense masses and bound the fibrillar silica gels together. A similar morphology was also noted in C_3S pastes carbonated either in pure CO_2 or air [25]. Despite possessing an elongated structure, the aragonite was noted to have a width of less than 100 nm. The small size and mainly dispersed nature of the $CaCO_3$ polymorphs within the matrices of the C-(A-)S-H samples prevented a peak separation of the elastic modulus distribution for $CaCO_3$. Instead, flakes of flattened cauliflower-like morphologies were predominant on both the surface and in the interior region of A0*-P-C (Fig. 7 (c) & (d)). The phase was assigned to vaterite incorporated in silica gels, and the observed morphology was due to space confinement and the resulting crystal growth restriction. Its adherence to the polymerized silica was postulated to provide a reinforcing action to the decalcified C-(A-)S-H. It is noted that EDS spectra for gold occurred in A0*-P-C as the compact was gold coated before the SEM analysis to

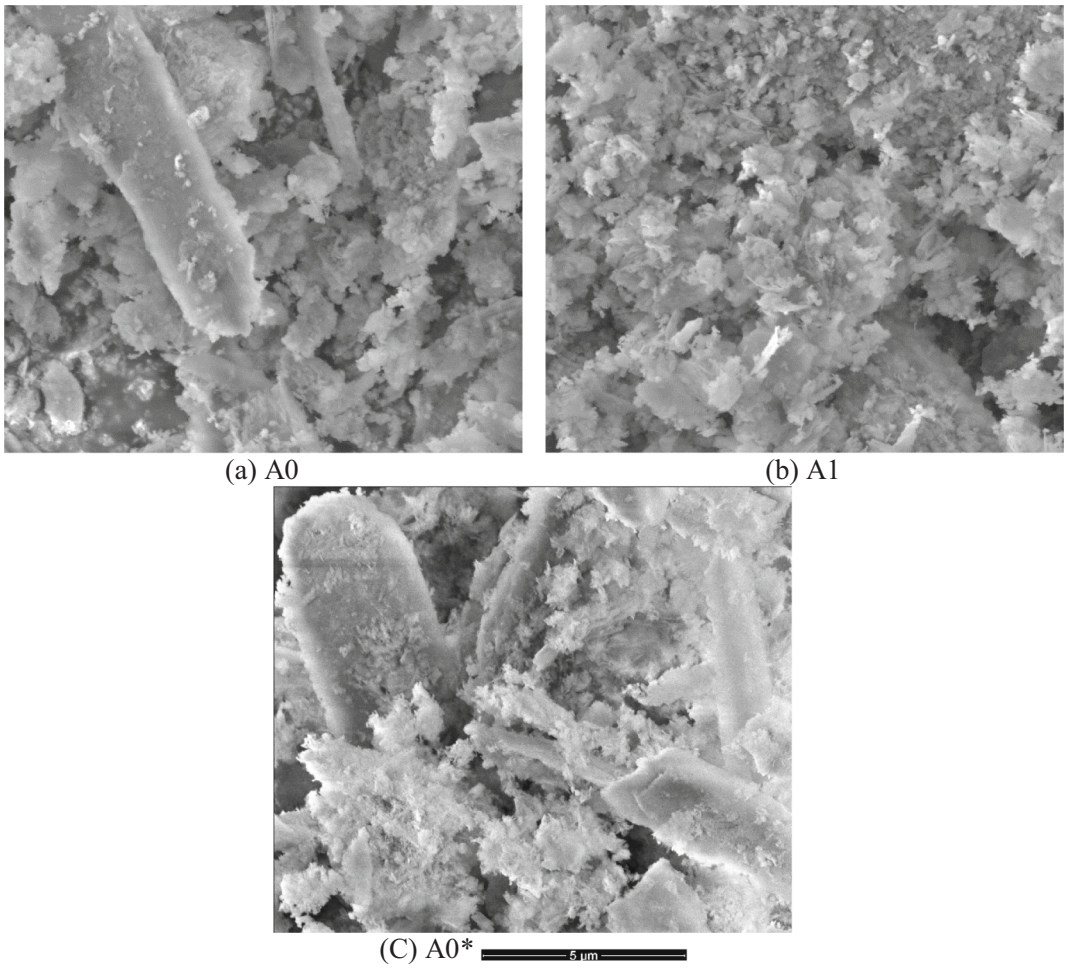

Fig. 6. SEM micrographs for: (a) C-S-H, (b) C-A-S-H under 11% RH at 22–24 °C (A0 and A1, respectively), and (c) C-S-H under 75% RH at 22–24 °C (A0*).

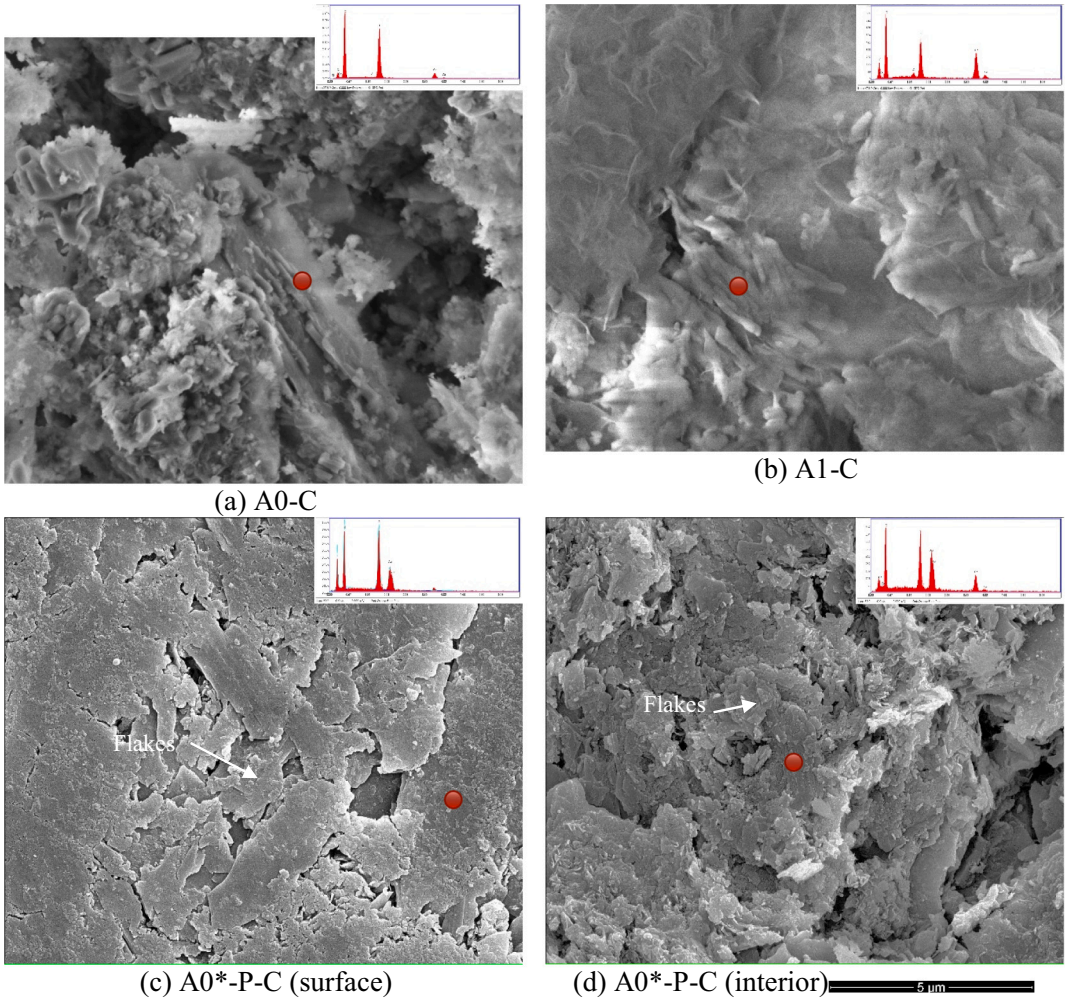

Fig. 7. SEM micrographs for samples under 20% CO_2 at 80% RH and 30 °C: (a) C-S-H (A0-C), (b) C-A-S-H (A1-C), (c) surface, and (d) exterior region of C-S-H compacted and carbonated (A0*-P-C).

prevent charging.

Fig. 8 (a–d) revealed the morphologies of selected C-(A-)S-H powders under TEM. It was observed that both A0 and A1 exhibited a foil-like nanoscale morphology (after dispersion). Folded foils were dominant in the A0 sample, which helped to explain the needle-like structure as observed in the SEM results. In comparison, the incorporation of Al in the A1 sample induced more cross-linking, enhancing the stiffness of the C-A-S-H sheets, thus leading to their more defined platelet structure. Under carbonation, silica gels formed, and their highly polymerized structure was reflected by the formation of larger and softer foils of a featureless morphology, consistent with the SEM images. Small fragments of $CaCO_3$ polymorphs were visible to be dispersed within the framework of the silica gels. The longer rod-like form of aragonite observed under SEM was not apparent here, attributed to its possible settlement in the dispersion medium (ethanol) due to its high density and large aspect ratio. The TEM results corroborated the formation of the amorphous silica gels with increased polymerization and nanoparticles embedded in the framework of the carbonated C-(A-)S-H.

As shown in Fig. 8 (e), C-S-H in A0*-P-C exhibited a different morphology in comparison to A0-C. Consistent with the SEM results, the silica gel foils were of smaller sizes and clustered to form smaller globules. A magnified image of the boxed region of Fig. 8 (e) is shown in Fig. 8 (f) and reveals that the silica gels were intermixed with nano-sized crystallites. The diffracted pattern (inset of Fig. 8 (f)) of the highlighted region was analyzed with ImageJ to identify the d-spacing according to the procedure outlined in [128]. The d-spacing values corresponding to the three visible diffraction rings were found to be 0.1668, 0.2562, and 0.2980 nm, which correspond to vaterite (amcsd 0004854), aragonite (amcsd 0000233), and calcite (amcsd 0000098), as also noted by other researchers [129,130]. These $CaCO_3$ crystallites acted as integral reinforcement of the amorphous silica, which contributed to the increase in the indentation modulus of A0*-P-C. They may also restrain the growth of the silica gels, leading to their smaller and less connected morphology.

3.4. N_2 adsorption and pore size distribution

The cumulative pore volume data derived from N_2 adsorption and desorption results for A0, A1, A0-C, A1-C, and A0*-P-C are given in Fig. 9. A0* was not tested considering its similarity to A0 upon drying at 150 °C as part of the degassing regime. The pore sizes in Fig. 9 were presented in the range of 2–100 nm as limited by the detection of the equipment. The range covered the hierarchical pore distribution in packed globules of C-(A-)S-H, which is composed of intraglobular or interlayer pores (<1 nm) between sheets, small gel pores (1–3 nm) between packed globules, and large gel pores (3–12 nm) in flocs of the globules [93,94]. Capillary pores in size range of 100 nm would also exist [44]. It is revealed that the initial sample pore volumes based on the nonlocal density functional theory (NLDFT) were not zero, indicating the existence of pores smaller than 2 nm in the C-(A-)S-samples.

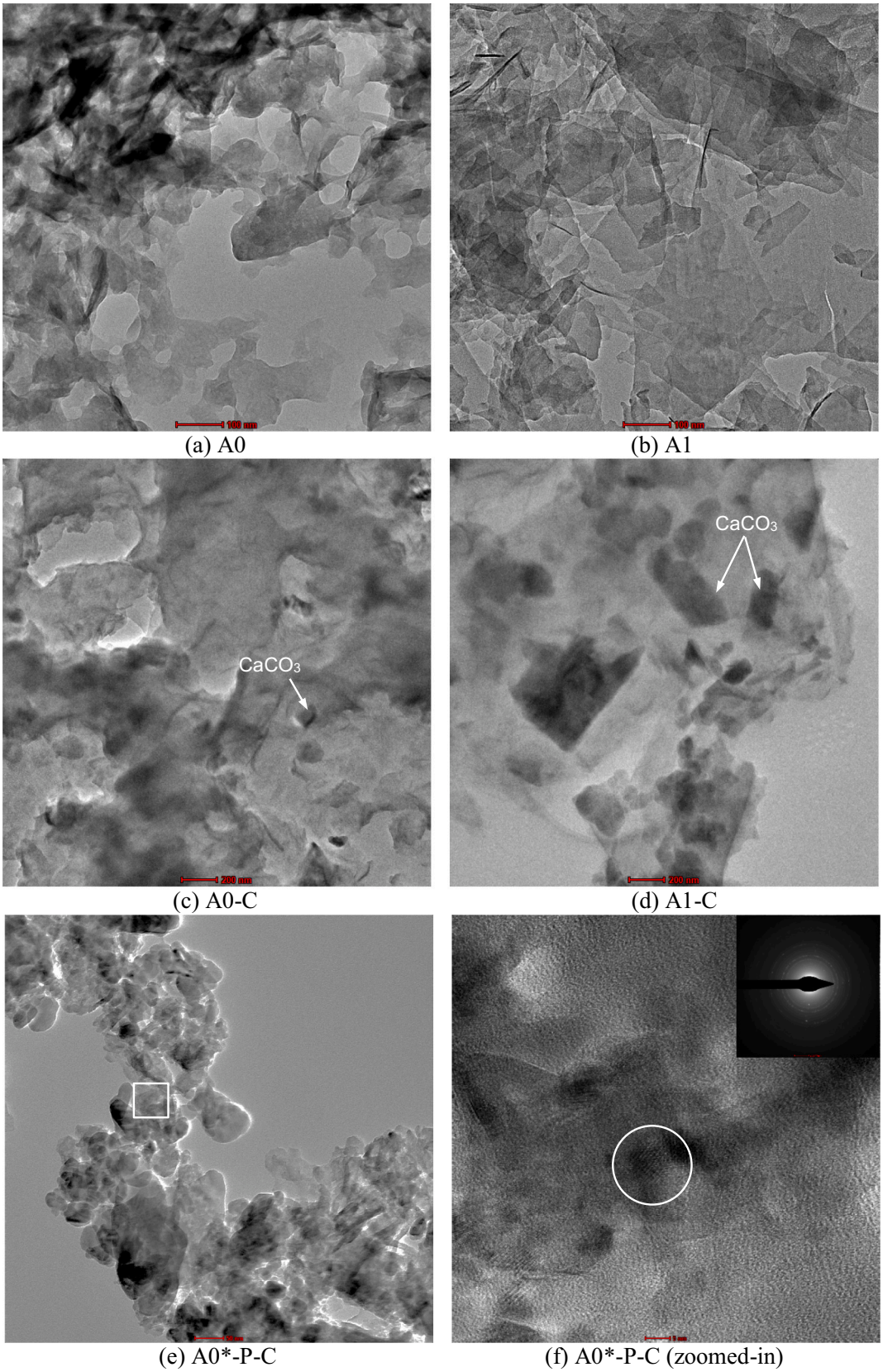

Fig. 8. Morphologies from TEM analysis for: (a) C-S-H, (b) C-A-S-H under 11% RH at 22–24 °C (A0 and A1, respectively), (c) C-S-H, (d) C-A-S-H under 20% CO_2 at 80% RH and 30 °C (A0-C and A1-C, respectively), (e) overview, and (f) zoomed-in images of C-S-H compacted and carbonated (A0*-P-C) of (e).

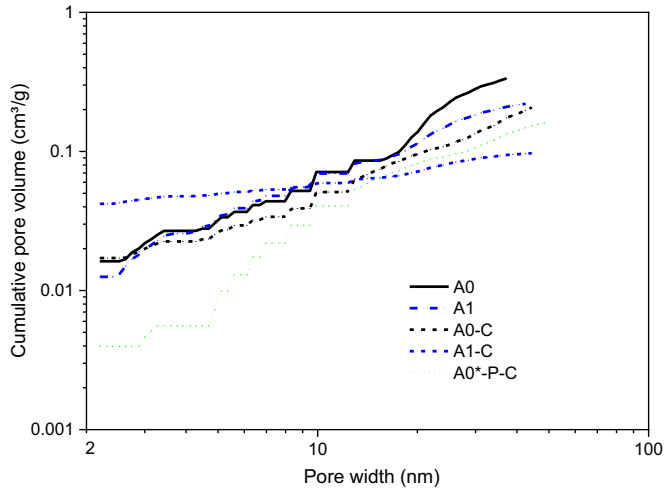

Fig. 9. Cumulative pore volume derived from N_2 adsorption-desorption for C-S-H (A0) and C-A-S-H (A1) under: (i) 11%, and (ii) 20% CO_2 at 80% RH (annotated by C).

A1 exhibited a lower initial pore volume in comparison to that of A0. This was attributable to the cross-linking induced by Al, thus limiting the amount of N_2 adsorbed between the interlayers. The enhanced polymerization and less folding morphology of C-A-S-H also helped explain the lower cumulative pore volume in A1. Carbonation induced decalcification from the interlayer and the defect sites and subsequent polymerization of silica gels. Yet, the formation of $CaCO_3$ polymorphs and their binding action led to a noticeable reduction in the total porosity and redistribution of pore sizes, as reflected by a lower slope of the cumulative pore volume curves. Despite the reduction in the overall pore volumes, A1-C exhibited a significant increase in pores <10 nm, as marked by a high initial cumulative pore volume at 2 nm. The increase was postulated to be caused by the linking and bridging induced by Al, leading to the formation of highly polymerized silica gels and reduced effectiveness of the binding action of $CaCO_3$ polymorphs. As expected, the densification and binding induced by the growth of $CaCO_3$ polymorphs under confinement led to more refinement and reduction in the gel pores and total porosity in A0*-P-C.

The specific surface areas (SSA) based on the Brunauer-Emmett-Teller (BET) theory [131] are summarized in Table 2. It is revealed that in comparison to A0, the cross-linking and enhanced polymerization in A1 with the incorporation of Al significantly reduced its specific surface area. Carbonation destroyed the interlayer structure, induced polymerization of silica gels, and precipitation $CaCO_3$ that bound the fibrous gels together, causing a reduction in the SSA of A0-C. The observation is consistent with the cumulative pore volume results and findings by other researchers [29]. The SSA values of hardened cement pastes ground to sizes of around 1 mm were also found to decrease with carbonation [132]. In contrast, under carbonation A1 exhibited an increase in the SSA from 82.6 m^2/g to 120.4 m^2/g in A1-C. Although further investigation is needed, the increase in the SSA for A1-C could be attributed to the enhanced polymerization by the tetrahedral $Al(-OSi)_4$ units, thus reducing the binding action of carbonates as confirmed by its more fibrous morphology as shown in Fig. 7. In this case, decalcification, found to increase the total surface areas in both Portland cement and C_3S pastes [133], played a more dominant role in controlling the SSA in A1-C. Consistent with the morphology and pore size distribution, the SSA for A0*-P-C was significantly reduced to 36.1 m^2/g.

Table 2
SSA for C-S-H (A0) and C-A-S-H (A1) under (i)11%, and (ii) 20% CO_2 at 80% RH (annotated by C) (m^2/g).

A0	A1	A0-C	A1-C	A0*-P-C
96.9	82.6	74.3	120.4	36.1

4. Discussion

4.1. Interplay between phases, morphologies, microstructure, and micromechanical properties

The findings presented thus far demonstrated a complex interaction between phases, morphologies, microstructure, and the resulting micromechanical properties of C-(A-)S-H. A1 or C-A-S-H with Al/(Al + Si) of 0.1 exhibited an enhanced micromechanical response in comparison to A0 or C-S-H, attributed to the Al-induced cross-linking and its improved compressibility [79]. SEM revealed that A1 exhibited a smaller size distribution of globules while TEM demonstrated its sheet-like structure in comparison to a folded-foil morphology of A0, which helps to explain the higher compressibility of A1. Under carbonation, polymerized silica and calcium carbonate ($CaCO_3$) polymorphs were formed. The morphology of the loose carbonated A0 and A1 was characterized by more fibrillar silica gels interspersed and bound by the $CaCO_3$ polymorphs. Despite the formation of $CaCO_3$, the matrix moduli of the corresponding compacts were significantly reduced due to the formation of the fibrous silica gels and submicron $CaCO_3$, rendering an absence of its modulus peak under nanoindentation. In contrast, the compacted pellet of C-S-H, which was subsequently carbonated and indented, attained a higher modulus response due to pore filling of the $CaCO_3$ polymorphs as a result of confinement. The carbonates also became integral with the silica gels to provide a reinforcing action. The two observations imply that decalcification induced by carbonation reduces the intrinsic micromechanical properties of loose C-(A-)S-H powders. Under confinement, such as in a typical concrete matrix, $CaCO_3$ is incorporated into the silica gels, resulting in an enhancement to the micromechanical properties of the system. This strengthening mechanism will ultimately improve the macro-scale mechanical response of the composite.

4.2. Implications for ordinary Portland cement composites and applications

This study unravels the fundamental change to the chemical, micromechanical, and morphological characteristics of C-(A-)S-H under carbonation. However, generalized implications of the study results on the response of paste and concrete matrices require careful consideration. First, the hydration products in concrete are a phase assemblage of C-(A-)S-H, $Ca(OH)_2$, ettringite, monosulfate, and unhydrated phases, which were shown to have different carbonation kinetics when exposed to CO_2 [42,134]. Also, a faster carbonation rate was noted in C-(A-)S-H with high Ca/Si ratios [42], which is further complicated by the early carbonation of the outer C-(A-)S-H products [135] and leaching or migration of Ca from the inner C-(A-)S-H products and unhydrated clinker grains into the matrix [136]. For Portland cement-based binders, the rate and extent of carbonation were found to depend on the replacement level, material, and hydration degree [134] with Portland Pozzolana Cement (PPC) and Limestone Calcined Clay Cement (LC^3) exhibiting an increase in porosity upon carbonation due to a lack of Ca $(OH)_2$ to $CaCO_3$ for pore filling [136].

Nanoindentation [81,113], high-pressure XRD [101,116], and atomic force microscopy [115] have been used to probe the micro and nanomechanical properties of C-(A-)S-H, whose nanostructure can be described as colloids of globules containing solid C-(A-)S-H, pores and water [93]. It turns out nanoindentation is a promising technique as it is able to capture the aggregate effects of the solid C-(A-)S-H and pores. In addition, other intermixed impurities such as $Ca(OH)_2$, shown to significantly increase the indentation elastic modulus [137], are within the interaction volume of the indentation tip. With the nanoindentation technique, our findings clearly demonstrated that carbonated C-(A-)S-H

experienced decalcification and reduced binding ability, as reflected in the reduction in the intrinsic elastic modulus of the C-(A-)S-H powders undergoing carbonation before compaction and indentation. As an analogy to paste or concrete matrices, a compacted C-(A-)S-H sample was prepared and subsequently carbonated before nanoindentation. The carbonates were found to reinforce the decalcified C-(A-)S-H and densified the matrix, leading to an enhancement to the composite modulus. It follows that carbonated C-(A-)S-H in concrete, i.e., under confinement, made of conventioanl PC would exhibit an improved mechanical performance to result in an enhanced macro-scale strength. However, in low Ca binders, the associated low $Ca(OH)_2$ content due to pozzolanic reactions and low Ca/Si in the C-(A-)S-H will produce fewer carbonates upon carbonation. As a result, the corresponding matrix under carbonation will be less dense, and the strength could be lower in comparison to ordinary PC-based composites. Thus, a coupling effect of decalcination and carbonate formation plays a critical role in governing the macroscale response of carbonated concrete matrices.

The significant carbonation content of C-(A-)S-H upon exposure to the CO_2 environment implies an inherent potential of hydrated cement to capture CO_2. In this regard, one potential application is the carbonation of recycled concrete aggregates (RCA) for both CO_2 sequestration and performance enhancement. Exposure of RCAs to a CO_2 environment was found to induce carbonation of $Ca(OH)_2$, C-S-H, and unhydrated cement minerals to form $CaCO_3$ and silica gels which fill the pores and microcracks to result in an improved microstructure and composite performance [138,139]. Owing to the large surface area of RCAs, smaller aggregates were found to achieve a significantly higher carbonation percentage [138]. Concrete fines with limestone contamination attained a CO_2 uptake capacity of 13 wt% [76]. Flue gas from cement plants was shown to be feasible for accelerated carbonation of RCAs to improve their quality for use in concrete [140]. It follows that concrete produced with binders requiring carbonation such as brucite precipitated from reject brine [141–144], wollastonite [145,146], and magnesium silicate [147,148] will adhere to the same strength development mechanism. The formation of carbonates and the subsequent pore filling under carbonation will contribute to the mechanical property development and structural integrity of the carbonated composites.

5. Conclusions

The study investigated the evolution of phases, micromechanical and morphological properties of synthetic calcium (alumino)silicate hydrates C-(A-)S-H under carbonation. Both powder and compacted samples were exposed to an accelerated carbonation regime of 20% CO_2, 80% relative humidity at 30 °C to simulate a long-term carbonation condition or concentrated CO_2 treatment of concrete products. In-depth analyses of thermal gravimetry, X-ray diffraction, Raman spectroscopy, nanoindentation, scanning electron microscopy, and transmission electron data were performed. Based on the results and discussion above, the following can be concluded:

- Under the carbonation, C-(A-)S-H decomposed due to decalcification at the interlayer and defects sites, leading to a disappearance of its crystallinity.
- High carbonation contents of 33.4% and 35.2% were achieved for both C-S-H and C-A-S-H powders, respectively.
- The carbonation regime led to a significant reduction in the intrinsic elastic modulus of the carbonated C-(A-)S-H as measured with compacted produced with the carbonated powders. In contrast, the C-(A-)S-H compacts followed by carbonation experienced a significant enhancement to the micromechanical properties due to the growth of carbonates under confinement and the resulting reinforcing action of the decalcified C-(A-)S-H and pore filling provided by $CaCO_3$ polymorphs.
- Despite the multi-phase formation, a single-modal distribution was apparent in the frequency plots of the indentation elastic modulus, attributed to the small sizes (<100 nm) of the carbonation products and their homogenous distribution within the system.
- For the carbonated C-(A-)S-H powders, a more fibrillar morphology was noted due to the formation of highly polymerized silica gels, while the $CaCO_3$ polymorphs were observed to hold the gels together to form agglomerates intermixed with the carbonates. In contrast, $CaCO_3$ nanocrystallites were observed to be integral in the structure of the silica gels of the carbonated compacts, imparting a reinforcing action and enhancement to the resulting micromechanical properties.
- The carbonation regime led to a noticeable reduction in the overall pore volume due to the polymerization of silica gels and the formation of dense masses of $CaCO_3$ polymorphs that bound the gels together. Yet, a higher content of the interlayer pores was observed in the aluminum-incorporated powder sample under carbonation, possibly attributable to its enhanced polymerization and the associated reduced effectiveness of the binding action of $CaCO_3$ polymorphs.

CRediT authorship contribution statement

Rotana Hay: Conceptualization, Methodology, Investigation, Writing - original draft, Writing-review & editing, Project administration

Jiaqi Li: Conceptualization, Investigation, Writing-review & editing

Kemal Celik: Conceptualization, Writing - review & editing, Supervision, Project administration, Funding acquisition.

Declaration of competing interest

The authors declare that they have no known competing financial interests or personal relationships that could have appeared to influence the work reported in this paper.

Acknowledgment

The authors are very grateful to Core Technology Platforms (CTPs) experts, specifically Dr. James Weston, Dr. Liang Li, and Dr. Renu Pasricha, for their guidance on some of the experiments. This work was supported by the NYUAD Center for Interacting Urban Networks (CITIES), funded by Tamkeen under the NYUAD Research Institute Award CG001, and by the Swiss Re Institute under the Quantum Cities™ initiative..

References

[1] H.F.W. Taylor, Cement Chemistry, Thomas Telford, 1997.
[2] L. Jiang, B. Lin, Y. Cai, A model for predicting carbonation of high-volume fly ash concrete, Cem. Concr. Res. 30 (2000) 699–702.
[3] J. Ibáñez, L. Artús, R. Cuscó, Á. López, E. Menéndez, M.C. Andrade, Hydration and carbonation of monoclinic C2S and C3S studied by raman spectroscopy, J. Raman Spectrosc. 38 (2007) 61–67.
[4] L. Black, K. Garbev, I. Gee, Surface carbonation of synthetic CSH samples: a comparison between fresh and aged CSH using X-ray photoelectron spectroscopy, Cem. Concr. Res. 38 (2008) 745–750.
[5] C.A. García-González, N. El Grouh, A. Hidalgo, J. Fraile, A.M. López-Periago, C. Andrade, C. Domingo, New insights on the use of supercritical carbon dioxide for the accelerated carbonation of cement pastes, J. Supercrit. Fluids 43 (2008) 500–509.
[6] L.J. Parrott, Damage caused by carbonation of reinforced concrete, Mater. Struct. 23 (1990) 230–234.
[7] S.K. Roy, K.B. Poh, D.O. Northwood, Durability of concrete: accelerated carbonation and weathering studies, Build. Environ. 34 (1999) 597–606.
[8] N.R. Short, P. Purnell, C.L. Page, Preliminary investigations into the supercritical carbonation of cement pastes, J. Mater. Sci. 36 (2001) 35–41.
[9] S.E. Pihlajavaara, Some results of the effect of carbonation on the porosity and pore size distribution of cement paste, Mater. Struct. 1 (1968) 521–527.
[10] B. Šavija, M. Luković, Carbonation of cement paste: understanding, challenges, and opportunities, Constr. Build. Mater. 117 (2016) 285–301.
[11] E. Farahi, P. Purnell, N.R. Short, Supercritical carbonation of calcareous composites: influence of curing, Cem. Concr. Compos. 43 (2013) 48–53.

[12] V.T. Ngala, C.L. Page, Effects of carbonation on pore structure and diffusional properties of hydrated cement pastes, Cem. Concr. Res. 27 (1997) 995–1007.
[13] B. Johannesson, P. Utgenannt, Microstructural changes caused by carbonation of cement mortar, Cem. Concr. Res. 31 (2001) 925–931.
[14] K. Kamimura, P.J. Sereda, E.G. Swenson, Changes in weight and dimensions in the drying and carbonation of Portland cement mortars, Mag. Concr. Res. 17 (1965) 5–14.
[15] T.C. Powers, A Hypothesis on Carbonation Shrinkage, 1962.
[16] J.J. Chen, J.J. Thomas, H.M. Jennings, Decalcification shrinkage of cement paste, Cem. Concr. Res. 36 (2006) 801–809.
[17] J. Jerga, Physico-mechanical properties of carbonated concrete, Constr. Build. Mater. 18 (2004) 645–652.
[18] J.A. Gonzalez, J.S. Algaba, C. Andrade, Corrosion of reinforcing bars in carbonated concrete, Br. Corros. J. 15 (1980) 135–139.
[19] R.R. Hussain, T. Ishida, M. Wasim, Experimental investigation of time dependent non-linear 3D relationship between critical carbonation depth and corrosion of steel in carbonated concrete, Corros. Eng. Sci. Technol. 46 (2011) 657–660.
[20] A.B. Revert, K. De Weerdt, K. Hornbostel, M.R. Geiker, Carbonation-induced corrosion: investigation of the corrosion onset, Constr. Build. Mater. 162 (2018) 847–856.
[21] O.S.B. Al-Amoudi, M. Rasheeduzzafar, Maslehuddin, carbonation and corrosion of rebars in salt contaminated OPC/PFA concretes, Cem. Concr. Res. 21 (1991) 38–50.
[22] L.J. Parrott, A study of carbonation-induced corrosion, Mag. Concr. Res. 46 (1994) 23–28.
[23] J.F. Young, R.L. Berger, J. Breese, Accelerated curing of compacted calcium silicate mortars on exposure to CO2, J. Am. Ceram. Soc. 57 (1974) 394–397.
[24] R. Ylmen, U. Jäglid, Carbonation of Portland cement studied by diffuse reflection fourier transform infrared spectroscopy, Int. J. Concr. Struct. Mater. 7 (2013) 119–125.
[25] G.W. Groves, A. Brough, I.G. Richardson, C.M. Dobson, Progressive changes in the structure of hardened C3S cement pastes due to carbonation, J. Am. Ceram. Soc. 74 (1991) 2891–2896.
[26] G.W. Groves, D.I. Rodway, I.G. Richardson, The carbonation of hardened cement pastes, Adv. Cem. Res. 3 (1990) 117–125.
[27] J. Li, Q. Yu, H. Huang, S. Yin, Effects of Ca/Si ratio, aluminum and magnesium on the carbonation behavior of calcium silicate hydrate, Materials 12 (2019) 1268.
[28] A.M. Dunster, An investigation of the carbonation of cement paste using trimethylsilylation, Adv. Cem. Res. 2 (1989) 99–106.
[29] A. Morandeau, M. Thiery, P. Dangla, Investigation of the carbonation mechanism of CH and CSH in terms of kinetics, microstructure changes and moisture properties, Cem. Concr. Res. 56 (2014) 153–170.
[30] H.F.W. Taylor, Tobermorite, jennite, and cement gel, Z. Kristallogr. Cryst. Mater. 202 (1992) 41–50.
[31] E. Bonaccorsi, S. Merlino, A.R. Kampf, The crystal structure of tobermorite 14 Å (plombierite), a C-S–H phase, J. Am. Ceram. Soc. 88 (2005) 505–512.
[32] F. Matsushita, Y. Aono, S. Shibata, Calcium silicate structure and carbonation shrinkage of a tobermorite-based material, Cem. Concr. Res. 34 (2004) 1251–1257.
[33] R.L. Berger, J.F. Young, K. Leung, Acceleration of hydration of calcium silicates by carbon dioxide treatment, Nat. Phys. Sci. 240 (1972) 16–18.
[34] M. Liu, S. Hong, Y. Wang, J. Zhang, D. Hou, B. Dong, Compositions and microstructures of hardened cement paste with carbonation curing and further water curing, Constr. Build. Mater. 267 (2021), 121724.
[35] Y. Li, W. Liu, F. Xing, S. Wang, L. Tang, S. Lin, Z. Dong, Carbonation of the synthetic calcium silicate hydrate (CSH) under different concentrations of CO2: chemical phases analysis and kinetics, J. CO2 Util. 35 (2020) 303–313.
[36] W. Liu, Y. Li, S. Lin, L. Tang, Z. Dong, F. Xing, B. Dong, S. Hong, Changes in chemical phases and microscopic characteristics of fly ash blended cement pastes in different CO2 concentrations, Constr. Build. Mater. 257 (2020), 119598.
[37] W. Liu, S. Lin, Y. Li, W. Long, Z. Dong, L. Tang, Slag blended cement paste carbonation under different CO2 concentrations: controls on mineralogy and morphology of products, Materials 13 (2020) 3404.
[38] B. Li, Z. Sun, K. Hu, J. Yang, Influence of carbonation on the volume change of hardened cement pastes, Constr. Build. Mater. 260 (2020), 119709.
[39] X. Xian, Y. Shao, Microstructure of cement paste subject to ambient pressure carbonation curing, Constr. Build. Mater. 296 (2021), 123652.
[40] B.J. Zhan, D.X. Xuan, C.S. Poon, K.L. Scrivener, Multi-scale investigation on mechanical behavior and microstructural alteration of C-S-H in carbonated alite paste, Cem. Concr. Res. 144 (2021), 106448.
[41] W. Liu, Y.-Q. Li, L.-P. Tang, Z.-J. Dong, XRD and 29Si MAS NMR study on carbonated cement paste under accelerated carbonation using different concentration of CO2, Mater. Today Commun. 19 (2019) 464–470.
[42] S. Steiner, B. Lothenbach, T. Proske, A. Borgschulte, F. Winnefeld, Effect of relative humidity on the carbonation rate of portlandite, calcium silicate hydrates and ettringite, Cem. Concr. Res. 135 (2020), 106116.
[43] M. Auroy, S. Poyet, P. Le Bescop, J.-M. Torrenti, T. Charpentier, M. Moskura, X. Bourbon, Comparison between natural and accelerated carbonation (3% CO2): impact on mineralogy, microstructure, water retention and cracking, Cem. Concr. Res. 109 (2018) 64–80.
[44] P. Mehta, P.J.M. Monteiro, Concrete: Microstructure, Properties, and Materials, 3rd ed., McGraw-Hill Professional, 2006.
[45] K. Celik, R. Hay, C.W. Hargis, J. Moon, Effect of volcanic ash pozzolan or limestone replacement on hydration of Portland cement, Constr. Build. Mater. 197 (2019) 803–812.
[46] K. Celik, Development and Characterization of Sustainable Self-Consolidating Concrete Containing High Volume of Limestone Powder and Natural or Calcined Pozzolanic Materials, University of California, Berkeley, Ann Arbor, 2015.
[47] D. Nied, C. Stabler, M. Zajac, Assessing the synergistic effect of limestone and metakaolin, in: Calcined Clays for Sustainable Concrete, Springer, 2015, pp. 245–251.
[48] S.S. Berriel, A. Favier, E.R. Domínguez, I.R.S. Machado, U. Heierli, K. Scrivener, F. M. Hernández, G. Habert, Assessing the environmental and economic potential of limestone calcined clay cement in Cuba, J. Clean. Prod. 124 (2016) 361–369.
[49] Y.C. Díaz, S.S. Berriel, U. Heierli, A.R. Favier, I.R.S. Machado, K.L. Scrivener, J.F. M. Hernández, G. Habert, Limestone calcined clay cement as a low-carbon solution to meet expanding cement demand in emerging economies, Dev. Eng. 2 (2017) 82–91.
[50] K. Scrivener, F. Martirena, S. Bishnoi, S. Maity, Calcined clay limestone cements (LC3), Cem. Concr. Res. 114 (2018) 49–56.
[51] J. Tang, S. Wei, W. Li, S. Ma, P. Ji, X. Shen, Synergistic effect of metakaolin and limestone on the hydration properties of Portland cement, Constr. Build. Mater. 223 (2019) 177–184.
[52] M. Thomas, J. Matthews, Carbonation of fly ash concrete, Mag. Concr. Res. 44 (1992) 217–228.
[53] S. Lammertijn, N. De Belie, Porosity, gas permeability, carbonation and their interaction in high-volume fly ash concrete, Mag. Concr. Res. 60 (2008) 535–545.
[54] Q. Wang, P. Yan, J. Yang, B. Zhang, Influence of steel slag on mechanical properties and durability of concrete, Constr. Build. Mater. 47 (2013) 1414–1420.
[55] L. Han-Seung, X.-Y. Wang, Evaluation of compressive strength development and carbonation depth of high volume slag-blended concrete, Constr. Build. Mater. 124 (2016) 45–54.
[56] Z. Giergiczny, Fly ash and slag, Cem. Concr. Res. 124 (2019), 105826.
[57] D. Zhang, X. Cai, Y. Shao, Carbonation curing of precast fly ash concrete, J. Mater. Civ. Eng. 28 (2016), 04016127.
[58] S. Hussain, D. Bhunia, S.B. Singh, Comparative study of accelerated carbonation of plain cement and fly-ash concrete, J. Building Eng. 10 (2017) 26–31.
[59] L. Mo, F. Zhang, M. Deng, F. Jin, A. Al-Tabbaa, A. Wang, Accelerated carbonation and performance of concrete made with steel slag as binding materials and aggregates, Cem. Concr. Compos. 83 (2017) 138–145.
[60] I.G. Richardson, The nature of CSH in hardened cements, Cem. Concr. Res. 29 (1999) 1131–1147.
[61] F. Pelisser, P.J.P. Gleize, A. Mikowski, Effect of the Ca/Si molar ratio on the micro/nanomechanical properties of synthetic CSH measured by nanoindentation, J. Phys. Chem. C 116 (2012) 17219–17227.
[62] P. Faucon, A. Delagrave, J.C. Petit, C. Richet, J.M. Marchand, H. Zanni, Aluminum incorporation in calcium silicate hydrates (C− S− H) depending on their Ca/Si ratio, J. Phys. Chem. B 103 (1999) 7796–7802.
[63] B. Lothenbach, K. Scrivener, R.D. Hooton, Supplementary cementitious materials, Cem. Concr. Res. 41 (2011) 1244–1256.
[64] Q. Wang, J. Feng, P. Yan, The microstructure of 4-year-old hardened cement-fly ash paste, Constr. Build. Mater. 29 (2012) 114–119.
[65] J.E. Oh, S.M. Clark, P.J.M. Monteiro, Does the Al substitution in C-S–H (I) change its mechanical property? Cem. Concr. Res. 41 (2011) 102–106.
[66] J.L. Provis, Alkali-activated materials, Cem. Concr. Res. 114 (2018) 40–48.
[67] X. Zhu, M. Zhang, K. Yang, L. Yu, C. Yang, Setting behaviours and early-age microstructures of alkali-activated ground granulated blast furnace slag (GGBS) from different regions in China, Cem. Concr. Compos. 114 (2020), 103782.
[68] R.J. Myers, E. L'Hôpital, J.L. Provis, B. Lothenbach, Effect of temperature and aluminium on calcium (alumino) silicate hydrate chemistry under equilibrium conditions, Cem. Concr. Res. 68 (2015) 83–93.
[69] E.M. Foley, J.J. Kim, M.M.R. Taha, Synthesis and nano-mechanical characterization of calcium-silicate-hydrate (CSH) made with 1.5 CaO/SiO 2 mixture, Cem. Concr. Res. 42 (2012) 1225–1232.
[70] J.J. Kim, E.M. Foley, M.M.R. Taha, Nano-mechanical characterization of synthetic calcium–silicate–hydrate (C–S–H) with varying CaO/SiO2 mixture ratios, Cem. Concr. Compos. 36 (2013) 65–70.
[71] R.F. Feldman, V.S. Ramachandran, Differentiation of interlayer and adsorbed water in hydrated Portland cement by thermal analysis, Cem. Concr. Res. 1 (1971) 607–620.
[72] Y. Suda, T. Saeki, T. Saito, Relation between chemical composition and physical properties of CSH generated from cementitious materials, J. Adv. Concr. Technol. 13 (2015) 275–290.
[73] A.M.N. Moudio, H.K. Tchakouté, D.L.V. Ngnintedem, F. Andreola, E. Kamseu, C. P. Nanseu-Njiki, C. Leonelli, C.H. Rüscher, Influence of the synthetic calcium aluminate hydrate and the mixture of calcium aluminate and silicate hydrates on the compressive strengths and the microstructure of metakaolin-based geopolymer cements, Mater. Chem. Phys. 124459 (2021).
[74] Y. Li, S. Zhang, R. Wang, Y. Zhao, C. Men, Effects of carbonation treatment on the crushing characteristics of recycled coarse aggregates, Constr. Build. Mater. 201 (2019) 408–420.
[75] N.T. Dung, R. Hay, A. Lesimple, K. Celik, C. Unluer, Influence of CO2 concentration on the performance of MgO cement mixes, Cem. Concr. Compos. 103826 (2020).
[76] H.-J. Ho, A. Iizuka, E. Shibata, H. Tomita, K. Takano, T. Endo, Utilization of CO2 in direct aqueous carbonation of concrete fines generated from aggregate recycling: influences of the solid–liquid ratio and CO2 concentration, J. Clean. Prod. 127832 (2021).
[77] R. Mi, G. Pan, Y. Li, T. Kuang, Carbonation degree evaluation of recycled aggregate concrete using carbonation zone widths, J. CO2 Util. 43 (2021), 101366.

[78] J. Li, W. Zhang, P.J.M. Monteiro, Preferred orientation of calcium aluminosilicate hydrate compacts: implications for creep and indentation, Cem. Concr. Res. 143 (2021), 106371.
[79] R. Hay, J. Li, K. Celik, Influencing factors on micromechanical properties of calcium (alumino) silicate hydrate C-(A-)S-H under nanoindentation experiment, Cem. Concr. Res. 134 (2020), 106088.
[80] Agilent Technologies, Nano Indenter G200 User's Guide Palo Alto, California, 2013.
[81] G. Constantinides, F.J. Ulm, K. Van Vliet, On the use of nanoindentation for cementitious materials, Mater. Struct. 36 (2003) 191–196.
[82] G. Constantinides, F.-J. Ulm, The nanogranular nature of C-S–H, J. Mech. Phys. Solids 55 (2007) 64–90.
[83] G.G. Litvan, Variability of the nitrogen surface area of hydrated cement paste, Cem. Concr. Res. 6 (1976) 139–143.
[84] J.J. Thomas, H.M. Jennings, A.J. Allen, The surface area of hardened cement paste as measured by various techniques, Concr. Sci. Eng. 1 (1999) 45–64.
[85] S. Mantellato, M. Palacios, R.J. Flatt, Impact of sample preparation on the specific surface area of synthetic ettringite, Cem. Concr. Res. 86 (2016) 20–28.
[86] G.G. Litvan, R.E. Myers, Surface area of cement paste conditioned at various relative humidities, Cem. Concr. Res. 13 (1983) 49–60.
[87] M.C.G. Juenger, H.M. Jennings, The use of nitrogen adsorption to assess the microstructure of cement paste, Cem. Concr. Res. 31 (2001) 883–892.
[88] Q. Jin, S.L. Hordern, Y. Tang, K.E. Kurtis, NOx sequestration by calcium aluminate cementitious materials, Cem. Concr. Res. 142 (2021), 106381.
[89] I. Odler, The BET-specific surface area of hydrated Portland cement and related materials, Cem. Concr. Res. 33 (2003) 2049–2056.
[90] E. L'Hôpital, B. Lothenbach, D.A. Kulik, K. Scrivener, Influence of calcium to silica ratio on aluminium uptake in calcium silicate hydrate, Cem. Concr. Res. 85 (2016) 111–121.
[91] F.J. Trojer, The crystal structure of parawollastonite, Z. Kristallogr. Cryst. Mater. 127 (1968) 291–308.
[92] H.M. Jennings, J.J. Thomas, J.S. Gevrenov, G. Constantinides, F.-J. Ulm, A multi-technique investigation of the nanoporosity of cement paste, Cem. Concr. Res. 37 (2007) 329–336.
[93] H.M. Jennings, Refinements to colloid model of CSH in cement: CM-II, Cem. Concr. Res. 38 (2008) 275–289.
[94] H.M. Jennings, A. Kumar, G. Sant, Quantitative discrimination of the nano-pore-structure of cement paste during drying: new insights from water sorption isotherms, Cem. Concr. Res. 76 (2015) 27–36.
[95] T.F. Sevelsted, J. Skibsted, Carbonation of C-S–H and C–A–S–H samples studied by 13C, 27Al and 29Si MAS NMR spectroscopy, Cem. Concr. Res. 71 (2015) 56–65.
[96] K. Scrivener, R. Snellings, B. Lothenbach, A Practical Guide to Microstructural Analysis of Cementitious Materials, CRC Press, 2016.
[97] S. Goto, K. Suenaga, T. Kado, M. Fukuhara, Calcium silicate carbonation products, J. Am. Ceram. Soc. 78 (1995) 2867–2872.
[98] E.T. Stepkowska, J.L. Perez-Rodriguez, M.J. Sayagues, J.M. Martinez-Blanes, Calcite, vaterite and aragonite forming on cement hydration from liquid and gaseous phase, J. Therm. 73 (2003) 247–269.
[99] M.-A. Popescu, R. Isopescu, C. Matei, G. Fagarasan, V. Plesu, Thermal decomposition of calcium carbonate polymorphs precipitated in the presence of ammonia and alkylamines, Adv. Powder Technol. 25 (2014) 500–507.
[100] J. Li, G. Geng, R. Myers, Y.-S. Yu, D. Shapiro, C. Carraro, R. Maboudian, P.J. M. Monteiro, The chemistry and structure of calcium (alumino) silicate hydrate: a study by XANES, ptychographic imaging, and wide- and small-angle scattering, Cem. Concr. Res. 115 (2019) 367–378.
[101] G. Geng, R.J. Myers, J. Li, R. Maboudian, C. Carraro, D.A. Shapiro, P.J. M. Monteiro, Aluminum-induced dreierketten chain cross-links increase the mechanical properties of nanocrystalline calcium aluminosilicate hydrate, Sci. Rep. 7 (2017) 44032.
[102] J.J. Thomas, A.J. Allen, H.M. Jennings, Structural changes to the calcium–silicate–hydrate gel phase of hydrated cement with age, drying, and resaturation, J. Am. Ceram. Soc. 91 (2008) 3362–3369.
[103] W.-S. Chiang, E. Fratini, P. Baglioni, D. Liu, S.-H. Chen, Microstructure determination of calcium-silicate-hydrate globules by small-angle neutron scattering, J. Phys. Chem. C 116 (2012) 5055–5061.
[104] L.J. Parrott, A Review of Carbonation in Reinforced Concrete, Cement and Concrete Association, Wexham Spring, 1987.
[105] L. Black, C. Breen, J. Yarwood, K. Garbev, P. Stemmermann, B. Gasharova, Structural features of C-S–H (I) and its carbonation in air—a raman spectroscopic study. Part II: carbonated phases, J. Am. Ceram. Soc. 90 (2007) 908–917.
[106] P.H.R. Borges, J.O. Costa, N.B. Milestone, C.J. Lynsdale, R.E. Streatfield, Carbonation of CH and C-S–H in composite cement pastes containing high amounts of BFS, Cem. Concr. Res. 40 (2010) 284–292.
[107] S. Martinez-Ramirez, M. Frías, C. Domingo, Micro-raman spectroscopy in white Portland cement hydration: long-term study at room temperature, J. Raman Spectrosc. 37 (2006) 555–561.
[108] K. Garbev, P. Stemmermann, L. Black, C. Breen, J. Yarwood, B. Gasharova, Structural features of C-S–H (I) and its carbonation in air—a raman spectroscopic study. Part I: fresh phases, J. Am. Ceram. Soc. 90 (2007) 900–907.
[109] M. Tarrida, M. Madon, B. Le Rolland, P. Colombet, An in-situ raman spectroscopy study of the hydration of tricalcium silicate, Adv. Cem. Based Mater. 2 (1995) 15–20.
[110] S. Ortaboy, J. Li, G. Geng, R.J. Myers, P.J.M. Monteiro, R. Maboudian, C. Carraro, Effects of CO2 and temperature on the structure and chemistry of C–(A–) S-H investigated by raman spectroscopy, RSC Adv. 7 (2017) 48925–48933.
[111] R.J. Kirkpatrick, J.L. Yarger, P.F. McMillan, Y. Ping, X. Cong, Raman spectroscopy of CSH, tobermorite, and jennite, Adv. Cem. Based Mater. 5 (1997) 93–99.
[112] H. Aguiar, J. Serra, P. González, B. León, Structural study of sol–gel silicate glasses by IR and raman spectroscopies, J. Non-Cryst. Solids 355 (2009) 475–480.
[113] G. Constantinides, F.-J. Ulm, The effect of two types of C-S-H on the elasticity of cement-based materials: results from nanoindentation and micromechanical modeling, Cem. Concr. Res. 34 (2004) 67–80.
[114] F.-J. Ulm, M. Vandamme, H.M. Jennings, J. Vanzo, M. Bentivegna, K. J. Krakowiak, G. Constantinides, C.P. Bobko, K.J. Van Vliet, Does microstructure matter for statistical nanoindentation techniques? Cem. Concr. Compos. 32 (2010) 92–99.
[115] C.A. Jones, Z.C. Grasley, J.A. Ohlhausen, Measurement of elastic properties of calcium silicate hydrate with atomic force microscopy, Cem. Concr. Compos. 34 (2012) 468–477.
[116] G. Geng, R.J. Myers, M.J.A. Qomi, P.J.M. Monteiro, Densification of the interlayer spacing governs the nanomechanical properties of calcium-silicate-hydrate, Sci. Rep. 7 (2017) 10986.
[117] J. Li, W. Zhang, P.J.M. Monteiro, Structure and intrinsic mechanical properties of nanocrystalline calcium silicate hydrate, ACS Sustain. Chem. Eng. 8 (2020) 12453–12461.
[118] J. Li, W. Zhang, P.J.M. Monteiro, Mechanical properties of struvite-K: a high-pressure X-ray diffraction study, Cem. Concr. Res. 136 (2020), 106171.
[119] C.J. Haecker, E.J. Garboczi, J.W. Bullard, R.B. Bohn, Z. Sun, S.P. Shah, T. Voigt, Modeling the linear elastic properties of Portland cement paste, Cem. Concr. Res. 35 (2005) 1948–1960.
[120] W. Wilson, L. Sorelli, A. Tagnit-Hamou, Automated coupling of NanoIndentation and quantitative energy-dispersive spectroscopy (NI-QEDS): a comprehensive method to disclose the micro-chemo-mechanical properties of cement pastes, Cem. Concr. Res. 103 (2018) 49–65.
[121] J. Han, G. Pan, W. Sun, C. Wang, D. Cui, Application of nanoindentation to investigate chemomechanical properties change of cement paste in the carbonation reaction, Sci. China Technol. Sci. 55 (2012) 616–622.
[122] A.V. Girao, I.G. Richardson, R. Taylor, R.M.D. Brydson, Composition, morphology and nanostructure of C-S–H in 70% white Portland cement–30% fly ash blends hydrated at 55° C, Cem. Concr. Res. 40 (2010) 1350–1359.
[123] E. Tajuelo Rodriguez, I.G. Richardson, L. Black, E. Boehm-Courjault, A. Nonat, J. Skibsted, Composition, silicate anion structure and morphology of calcium silicate hydrates (CSH) synthesised by silica-lime reaction and by controlled hydration of tricalcium silicate (C3S), Adv. Appl. Ceram. 114 (2015) 362–371.
[124] J. Li, W. Zhang, K. Xu, P.J.M. Monteiro, Fibrillar calcium silicate hydrate seeds from hydrated tricalcium silicate lower cement demand, Cem. Concr. Res. 137 (2020), 106195.
[125] H.M. Jennings, B.J. Dalgleish, P. Pratt, Morphological development of hydrating tricalcium silicate as examined by electron microscopy techniques, J. Am. Ceram. Soc. 64 (1981) 567–572.
[126] Ö. Cizer, K.Van Balen, J. Elsen, D.Van Gemert, in: Crystal Morphology of the Precipitated Calcite Crystals From Accelerated Carbonation of Lime Binders, University of Rome, 2008, pp. 149–158.
[127] G.-T. Zhou, Q.-Z. Yao, S.-Q. Fu, Y.-B. Guan, Controlled crystallization of unstable vaterite with distinct morphologies and their polymorphic transition to stable calcite, Eur. J. Mineral. 22 (2010) 259–269.
[128] R. Taylor, A. Sakdinawat, S.R. Chae, H.R. Wenk, P. Levitz, R. Sougrat, P.J. M. Monteiro, Developments in TEM nanotomography of calcium silicate hydrate, J. Am. Ceram. Soc. 98 (2015) 2307–2312.
[129] D.B. Trushina, T.V. Bukreeva, M.V. Kovalchuk, M.N. Antipina, CaCO3 vaterite microparticles for biomedical and personal care applications, Mater. Sci. Eng. C 45 (2014) 644–658.
[130] J.D. Rodriguez-Blanco, K.K. Sand, L.G. Benning, ACC and vaterite as intermediates in the solution-based crystallization of CaCO 3, in: New Perspectives on Mineral Nucleation and Growth, Springer, 2017, pp. 93–111.
[131] K.S.W. Sing, Reporting physisorption data for gas/solid systems with special reference to the determination of surface area and porosity (Recommendations 1984), Pure Appl. Chem. 57 (1985) 603–619.
[132] J.J. Thomas, J. Hsieh, H.M. Jennings, Effect of carbonation on the nitrogen BET surface area of hardened Portland cement paste, Adv. Cem. Based Mater. 3 (1996) 76–80.
[133] J.J. Thomas, J.J. Chen, A.J. Allen, H.M. Jennings, Effects of decalcification on the microstructure and surface area of cement and tricalcium silicate pastes, Cem. Concr. Res. 34 (2004) 2297–2307.
[134] J. Herterich, Microstructure and Phase Assemblage of Low-clinker Cements During Early Stages of Carbonation, 2017.
[135] C. Sun, L. Liu, Y. Du, Analyses of Decalcification Process of Calcium Silicate Hydrate (CSH) Phase, IOP Publishing, 2019, pp. 022050.
[136] V. Shah, K. Scrivener, B. Bhattacharjee, S. Bishnoi, Changes in microstructure characteristics of cement paste on carbonation, Cem. Concr. Res. 109 (2018) 184–197.
[137] J.J. Chen, L. Sorelli, M. Vandamme, F.J. Ulm, G. Chanvillard, A coupled nanoindentation/SEM-EDS study on low water/cement ratio Portland cement paste: evidence for C-S–H/Ca(OH)2 nanocomposites, J. Am. Ceram. Soc. 93 (2010) 1484–1493.
[138] B. Zhan, C.S. Poon, Q. Liu, S. Kou, C. Shi, Experimental study on CO2 curing for enhancement of recycled aggregate properties, Constr. Build. Mater. 67 (2014) 3–7.
[139] C. Shi, Y. Li, J. Zhang, W. Li, L. Chong, Z. Xie, Performance enhancement of recycled concrete aggregate–a review, J. Clean. Prod. 112 (2016) 466–472.

[140] Y. Pu, L. Li, Q. Wang, X. Shi, L. Fu, G. Zhang, C. Luan, A.E.-F. Abomohra, Accelerated carbonation treatment of recycled concrete aggregates using flue gas: a comparative study towards performance improvement, J. CO2 Util. 43 (2021), 101362.
[141] H. Dong, C. Unluer, E.-H. Yang, A. Al-Tabbaa, Recovery of reactive MgO from reject brine via the addition of NaOH, Desalination 429 (2018) 88–95.
[142] F. Sun, Investigation of Mechanical Properties and Associated Microstructure of Reactive Magnesia Cement Synthesized From Reject Brine, 2018.
[143] I. Singh, R. Hay, K. Celik, Recovery and direct carbonation of brucite from desalination reject brine for use as a construction material 152, Cement and Concrete Research, 2022, 106673.
[144] S. Ruan, E.-H. Yang, C. Unluer, Production of reactive magnesia from desalination reject brine and its use as a binder, J. CO2 Util. (2021), 101383.
[145] W.J.J. Huijgen, G.-J. Witkamp, R.N.J. Comans, Mechanisms of aqueous wollastonite carbonation as a possible CO2 sequestration process, Chem. Eng. Sci. 61 (2006) 4242–4251.
[146] Solidia Technologies, Solidia Solutions, 2021.
[147] J. Fagerlund, S. Teir, E. Nduagu, R. Zevenhoven, Carbonation of magnesium silicate mineral using a pressurised gas/solid process, Energy Procedia 1 (2009) 4907–4914.
[148] E. Eikeland, A.B. Blichfeld, C. Tyrsted, A. Jensen, B.B. Iversen, Optimized carbonation of magnesium silicate mineral for CO2 storage, ACS Appl. Mater. Interfaces 7 (2015) 5258–5264.